

TotalSegmentator MRI: Sequence-Independent Segmentation of 59 Anatomical Structures in MR images

Tugba Akinci D'Antonoli MD¹, Lucas K. Berger¹, Ashraya K. Indrakanti¹, Nathan Vishwanathan¹, Jakob Weiß MD², Matthias Jung MD², Zeynep Berkarda MD², Alexander Rau MD², Marco Reisert PhD², Thomas Küstner PhD³, Alexandra Walter^{4,5}, Elmar M. Merkle MD¹, Martin Segeroth MD¹, Joshy Cyriac MSc¹, Shan Yang PhD¹, Jakob Wasserthal PhD¹

¹ Clinic of Radiology and Nuclear Medicine, University Hospital Basel, Basel, Switzerland

² University Medical Center Freiburg, Freiburg, Germany

³ Medical Image and Data Analysis (MIDAS.lab), University Hospital of Tuebingen, Tuebingen, Germany

⁴ Department of Medical Physics in Radiation Oncology, German Cancer Research Center, Heidelberg, Germany

⁵ Scientific Computing Center, Karlsruhe Institute of Technology, Karlsruhe, Germany

Corresponding author: jakob.wasserthal@usb.ch

Abstract

Purpose

To develop an open-source and easy-to-use segmentation model that can automatically and robustly segment most major anatomical structures in MR images independently of the MR sequence.

Materials and Methods

In this study we extended the capabilities of TotalSegmentator to MR images. 298 MR scans and 227 CT scans were used to segment 59 anatomical structures (20 organs, 18 bones, 11 muscles, 7 vessels, 3 tissue types) relevant for use cases such as organ volumetry, disease characterization, and surgical planning. The MR and CT images were randomly sampled from routine clinical studies and thus represent a real-world dataset (different ages, pathologies, scanners, body parts, sequences, contrasts, echo times, repetition times, field strengths, slice thicknesses and sites). We trained an nnU-Net segmentation algorithm on this dataset and calculated Dice similarity coefficients (Dice) to evaluate the model's performance.

Results

The model showed a Dice score of 0.824 [CI: 0.801, 0.842] on the test set, which included a wide range of clinical data with major pathologies. The model significantly outperformed two other publicly available segmentation models (Dice score, 0.824 versus 0.762; $p < 0.001$ and 0.762 versus 0.542; $p < 0.001$). On the CT image test set of the original TotalSegmentator paper it almost matches the performance of the original TotalSegmentator (Dice score, 0.960 versus 0.970; $p < 0.001$).

Conclusion

Our proposed model extends the capabilities of TotalSegmentator to MR images. The annotated dataset (<https://zenodo.org/doi/10.5281/zenodo.11367004>) and open-source toolkit (<https://www.github.com/wasserth/TotalSegmentator>) are publicly available.

1. Introduction

Magnetic Resonance Imaging (MRI) is an indispensable tool in diagnostic imaging, providing detailed images of the human body without the use of ionizing radiation. This advanced imaging technique relies on magnetic fields and radiofrequency pulses to produce detailed images essential for diagnosing a range of medical conditions, from neurological disorders to musculoskeletal injuries. While MRI offers unparalleled detail, the manual segmentation of these images requires intensive effort by radiologists, a process that is time-consuming, subject to interrater variability, and prone to errors.

The advent of automated image segmentation techniques has shown promise in addressing these limitations. One notable advancement in medical image segmentation is the development of nnU-Net, a self-configuring framework that has set new standards in medical image segmentation, which adapts to any new dataset with minimal user intervention, automatically adjusting its architecture, preprocessing, and training strategies to optimize performance (1,2) Tools such as TotalSegmentator, explored the capabilities of nnU-Net so far on CT images and proved to be very robust and widely used by the medical imaging community (3). These automated systems can potentially reduce the workload of radiologists, minimize human errors, and provide more consistent and reproducible results, and can have several clinical applications, such as treatment planning or disease progression monitoring, as well as supporting the newly developing field of opportunistic screening (4).

Despite these advancements in the field of segmentation of CT images, several challenges remain for the segmentation of MR images. One significant issue is the variation in the MRI exams due to different imaging parameters and protocols used across different sequences and body parts, which can affect the generalizability and accuracy of segmentation algorithms (5). Moreover, while existing algorithms perform well on some high-resolution sequences where structures are well-defined with high contrast, they struggle with different sequence types and pathologically altered anatomical structures where delineation is less clear. These factors highlight the need for ongoing research to enhance the robustness and reliability of automated MRI segmentation tools that could work across all sequences and all anatomical structures.

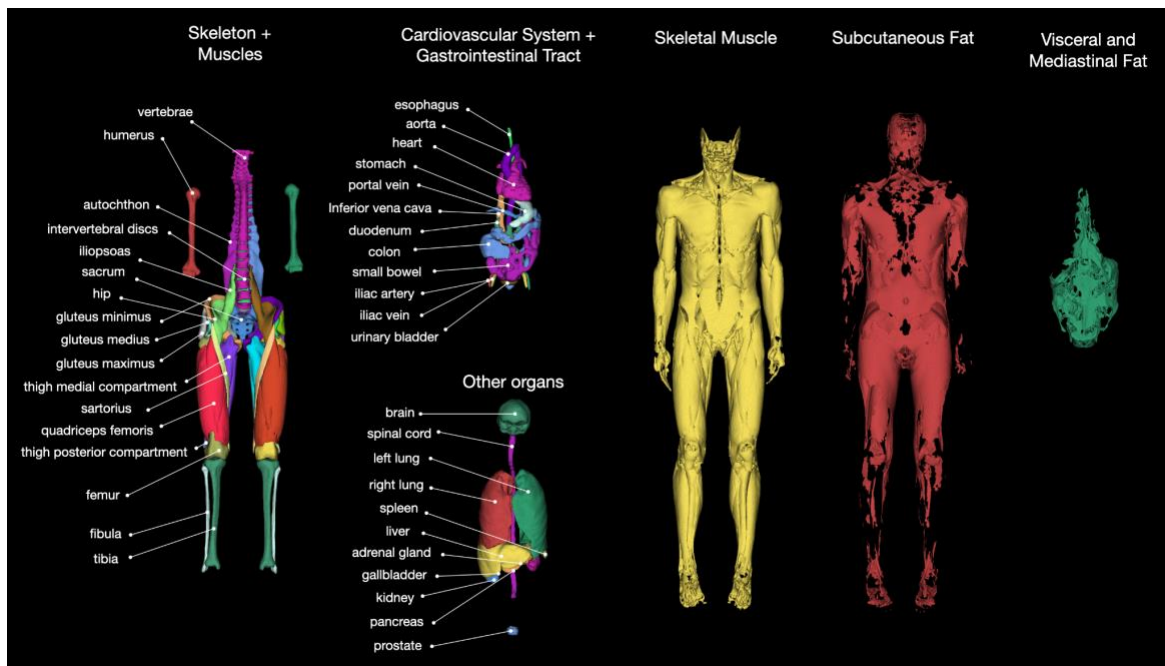


Figure 1: Overview of supported anatomical structures

In this study, we aim to develop and validate a novel open-source, easy-to-use segmentation model, which extends the capabilities of TotalSegmentator to MRI images of any type. We hope that our model can be easily integrated into existing clinical workflows and can operate in real-time to assist radiologists during diagnostic processes and employed in various research projects. By addressing these specific challenges, we intend to make contributions to the field of medical imaging segmentation.

1. Materials and Methods

The ethics waiver for this retrospective study was approved by the Ethics Committee Northwest and Central Switzerland (EKNZ BASEC Req-2022-00495).

2.1. Datasets

To generate a comprehensive and highly variant dataset, 251 MR examinations were randomly sampled from the years 2011 to 2023 from the University Hospital Basel picture archiving and communication system (PACS). For each examination the MR series was sampled randomly to obtain a high variety of data with different kinds of MR sequences (see results section for details). Additionally, we added 47 MR images from Imaging Data Commons (IDC) (6) to increase the image diversity (Supplemental Materials S4). To make the model more robust we also added 227 random CT images from the TotalSegmentator dataset. We did not add the entire TotalSegmentator dataset with over 1200 images to keep the dataset balanced with regards to the MR images. This resulted in a dataset of 525 images. This dataset was split into 495 training images and 30 test images (the test dataset only contains MR images). Since we did not perform hyperparameter optimization but relied on the nnU-Net default values, we did not use an additional validation set. As an external validation dataset we used the 20 MR validation images from the AMOS22 challenge (11) (dataset available at: <https://zenodo.org/records/7262581>).

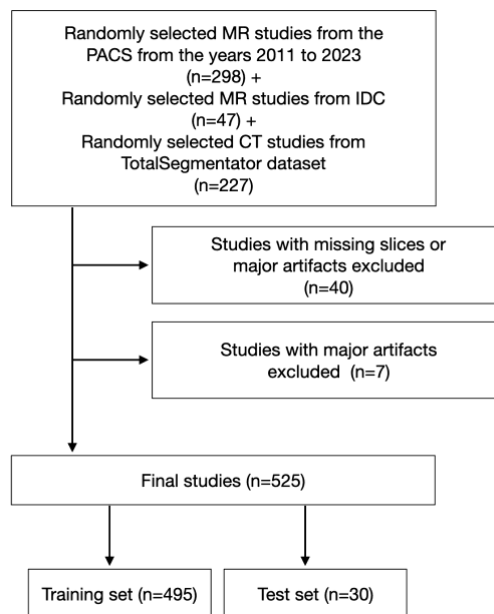


Figure 2: Diagram showing the inclusion of patients into the study.

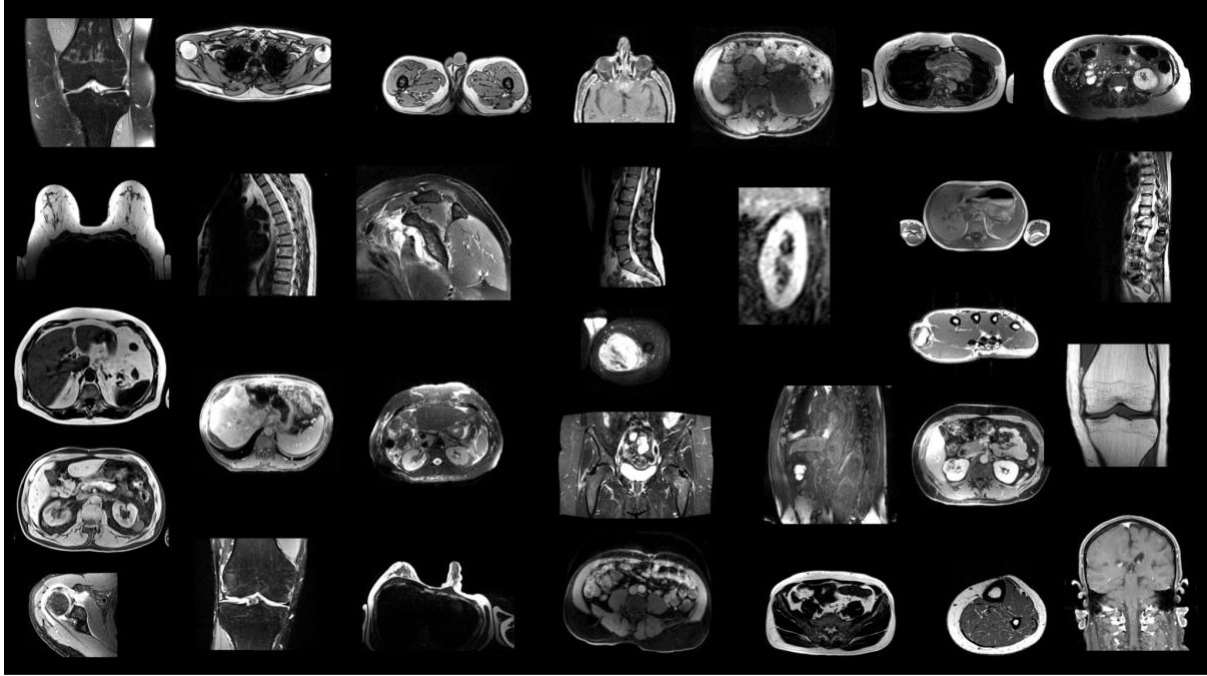


Figure 3: Exemplary overview of MR images in the training dataset. Since images were randomly sampled from the clinical routine it contains a wide variety of different contrasts, pathologies and image types.

2.2. Data Annotation

We identified 59 anatomical structures for segmentation (Figure 1; Supplemental Materials S1). The Nora Imaging Platform was used for manual segmentation or further refinement of generated segmentations (12). Segmentation was supervised by a board-certified radiologist (TAD) with 12 years of experience. If an existing model for a given structure was publicly available (Supplemental Materials S2), that model was used to create the first segmentation, which was then validated and refined manually (7,8).

To speed the process further, we used an iterative learning approach, as follows. After manual segmentation of the first 10 patients was completed, a preliminary nnU-Net was trained, and its predictions were manually refined, if necessary. Retraining of the nnU-Net was performed after reviewing and refining 125 additional patients. In the end, all 298 MR scans had annotations that were manually reviewed and corrected if necessary. These final annotations served as the ground truth for training and testing. This final model was independent of the intermediate models trained during the annotation workflow, which reduced bias in the test set to a minimum.

2.3. Model

We used the model from the nnU-Net framework, which is a U-Net–based implementation that automatically configures all hyperparameters based on the dataset characteristics (1,2). One model was trained on MR+CT scans with 1.5 mm isotropic resolution. To allow for lower technical requirements (random-access memory [RAM] and graphics processing unit [GPU] memory), we also trained a second model on 3 mm isotropic resolution (for more details on the training, see Supplemental Materials S5).

Since the tissue types skeletal muscle, subcutaneous fat and torso fat overlap with other classes we trained these three in a separate model. Training one model with 1.5 mm resolution and 56 classes

would require more RAM than typical workstations have available. Therefore we split this model into two models with each 28 classes.

We only trained one model (instead of training 5 models on 5 folds and then ensembling these) to keep the inference runtime low. For most applications this is more important than a slightly increased Dice score.

The runtime for the prediction of one case was measured on a local workstation with an Intel Core i9 3.5GHz CPU and Nvidia GeForce RTX 3090 GPU.

2.4. Baseline Models

We compared against the following two publicly available baseline models: (1) The tool MRSegmentator (8) and (2) a nnU-Net (“AMOS”) trained on the AMOS22 challenge training dataset (11). Comparison was limited to 40 structures for MRSegmentator and 13 structures for AMOS (Supplemental Materials S3). For fair comparison we did not ensemble results for all 5 training folds for MRSegmentator and AMOS as this was also not done for TotalSegmentator to reduce inference runtime.

2.5. Statistical Analysis

As evaluation metrics, the Dice similarity coefficient (Dice), a commonly used spatial overlap index, and the normalised surface distance (NSD), which measures how often the surface distance is <3 mm, were calculated between the predicted segmentations and the human approved ground truth segmentations as recommended (9,10). Both metrics range between 0 (worst) and 1 (best) and were calculated on the test set. For additional evaluation, we compared our model also on the test set from the original TotalSegmentator paper containing CT images.

Normal distribution of Dice and NSD was rejected by using the Kolmogorov-Smirnov test. Continuous variables were reported as pseudomedian and associated 95% confidence intervals (CI) using an underlying signed rank distribution. Wilcoxon signed rank test was used for model comparison with an alpha level of 0.05. All statistical analyses were performed using Python 3.9.

3. Results

3.1. Characteristics of the Study Sample

Data regarding basic demographic characteristics of patients included in the training dataset of 298 MR images are shown in Table 1 and Figure 4. The dataset contained a high variety of MR images, with differences in contrast, slice thickness, field strength, acquisition sequences (e.g. T1, T2, PD), echo time, repetition time, resolution, and contrast agent. Three different manufacturers, as well as MR images from 4 different sites and 30 different scanners were included in the dataset. The additional 227 CT images were randomly sampled from the Totalsegmentator dataset and follow the distributions shown in Figure 3 of the TotalSegmentator paper (3).

	MR data (n=298)	CT data (n=227)
Median age (years)	60.0 (IQR: 47.0-71.0)	69.0 (IQR: 61.0-77.0)
Nr of males	147	74
Nr of females	104	61
Nr with unknown sex	47	92

Table 1: Demographic characteristics of the study population.

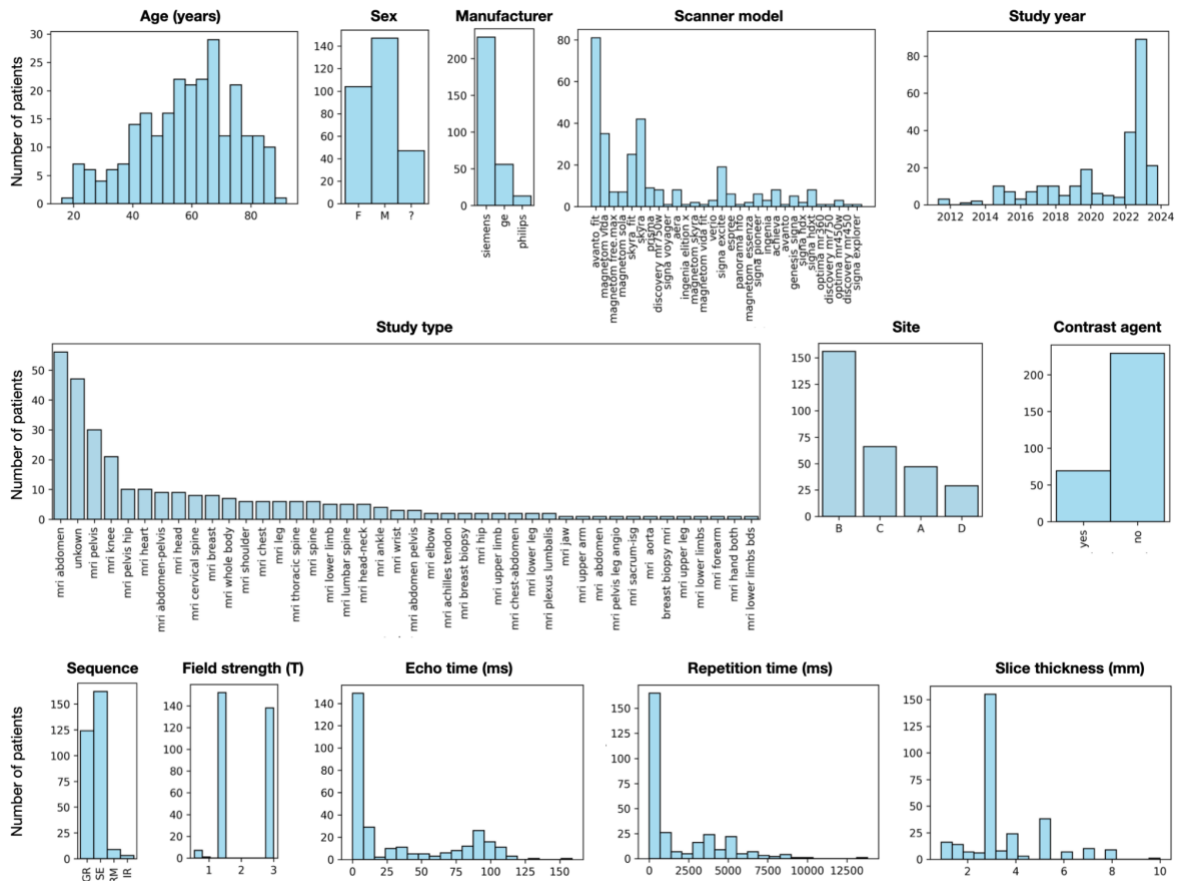


Figure 4: Histograms showing the distribution of different parameters of the training dataset, demonstrating the dataset's high diversity.

3.2. Segmentation Evaluation

The model trained on MR and CT images with their original resolution showed a Dice score of 0.824 [CI: 0.801, 0.842], and a NSD of 0.882 [CI: 0.860, 0.900]. The 3 mm model showed a lower Dice score of 0.724 [CI: 0.683, 0.757], but a NSD of 0.799 [CI: 0.760, 0.827]. Results for each structure independently are shown in Figure S1 and at https://github.com/wasserth/TotalSegmentator/blob/master/resources/results_all_classes_mr.json

In a direct comparison of our model to the MRSegmentator, our model achieved a significantly higher Dice score (0.824 [CI: 0.796, 0.848] vs 0.762 [CI: 0.733, 0.787]); $p < 0.001$) and NSD score (0.889 [CI: 0.859, 0.913] vs 0.824 [CI: 0.792, 0.856]; $p < 0.001$).

For a fair comparison with the AMOS model, only the 13 abdominal structures supported by AMOS were evaluated. Our model demonstrated significantly higher performance than the AMOS model, with a Dice score of 0.762 (CI: 0.692, 0.806) compared to AMOS's 0.512 (CI: 0.458, 0.596), and an NSD of 0.826 (CI: 0.745, 0.871) versus AMOS's 0.575 (CI: 0.499, 0.650); both comparisons yielded $p < 0.001$. When limited to the 13 structures supported by AMOS, MRSegmentator outperformed TotalSegmentator MRI by 2 points in Dice score (0.782 [CI: 0.742, 0.817] vs 0.762 [CI: 0.692, 0.806]; $p < 0.001$). This indicates that MRSegmentator excels at segmenting abdominal organs, but faces challenges with some of the other structures. This observation is confirmed on the external AMOS MR validation dataset: TotalSegmentator showed a Dice of 0.801 [CI: 0.780, 0.824] and a NSD of 0.883 [CI: 0.866, 0.897], while MRSegmentator had a Dice of 0.836 [CI: 0.815, 0.856] and a NSD of 0.924 [CI: 0.910, 0.938]. AMOS showed a Dice of 0.907 [CI: 0.893, 0.919] and a NSD of 0.972 [CI: 0.965, 0.978]. The better performance of both TotalSegmentator MRI and MRSegmentator on the AMOS validation data compared to our test set is mainly due to the better image quality of the AMOS data. Our dataset comprises more diverse clinical images, including lower resolution, varying orientations, and low contrast (see Figure 4). The high performance of the AMOS model on the AMOS validation data can be explained by a high similarity between the AMOS training and validation dataset. But the AMOS model does not generalise to more diverse data as shown by the low performance on our test set.

On the CT test set the original TotalSegmentator CT performs best (Dice: 0.970 [CI: 0.969, 0.971], NSD: 0.997 [CI: 0.996, 0.997]), followed by the proposed TotalSegmentator MRI (Dice: 0.960 [CI: 0.959, 0.962], NSD: 0.994 [CI: 0.993, 0.994]), MRSegmentator (Dice: 0.944 [CI: 0.942, 0.946], NSD: 0.984 [CI: 0.982, 0.985]) and AMOS (Dice: 0.907 [CI: 0.901, 0.913], NSD: 0.959 [CI: 0.954, 0.964]). Table 2 gives an overview of all results.

	Nr of classes	Dice	NSD
MR test set			
TotalSegmentator MRI	59	0.824 [CI: 0.801, 0.842]	0.882 [CI: 0.860, 0.900]
TotalSegmentator MRI 3mm	59	0.724 [CI: 0.683, 0.757]	0.799 [CI: 0.760, 0.827]
TotalSegmentator MRI	40	0.824 [CI: 0.796, 0.848]	0.889 [CI: 0.859, 0.913]
MRSegmentator	40	0.762 [CI: 0.733, 0.787]	0.824 [CI: 0.792, 0.856]
TotalSegmentator MRI	13	0.762 [CI: 0.692, 0.806]	0.826 [CI: 0.745, 0.871]
MRSegmentator	13	0.782 [CI: 0.742, 0.817]	0.844 [CI: 0.797, 0.883]
AMOS	13	0.542 [CI: 0.475, 0.606]	0.619 [CI: 0.557, 0.681]

CT test set			
TotalSegmentator MRI	40	0.960 [CI: 0.959, 0.962]	0.994 [CI: 0.993, 0.994]
TotalSegmentator CT	40	0.970 [CI: 0.969, 0.971]	0.997 [CI: 0.996, 0.997]
MRSegmentator	40	0.944 [CI: 0.942, 0.946]	0.984 [CI: 0.982, 0.985]
TotalSegmentator MRI	13	0.950 [CI: 0.947, 0.953]	0.992 [CI: 0.990, 0.993]
MRSegmentator	13	0.943 [CI: 0.939, 0.947]	0.990 [CI: 0.988, 0.992]
AMOS	13	0.907 [CI: 0.901, 0.913]	0.959 [CI: 0.954, 0.964]
AMOS MR test set			
TotalSegmentator MRI	13	0.801 [CI: 0.780, 0.824]	0.883 [CI: 0.866, 0.897]
MRSegmentator	13	0.836 [CI: 0.815, 0.856]	0.924 [CI: 0.910, 0.938]
AMOS	13	0.907 [CI: 0.893, 0.919]	0.972 [CI: 0.965, 0.978]

Table 2: Overview of results on our proposed model and the baseline models on the MR and the CT test set (NSD: Normalised Surface Distance; CI: 95% Confidence Interval)

3.3. Ablation study

We trained two additional models: one solely on MR images and another solely on CT images from our training dataset. Our proposed model, which was trained on both MR and CT images, demonstrated significantly better performance on the MR test set compared to the model trained exclusively on MR images. This indicates that incorporating CT images enhances MR segmentation. Conversely, on the CT test set, the model trained exclusively on CT images slightly outperformed the combined MR+CT model. This suggests that focusing on standardised HU values in CT images aids the model, while the inclusion of MR images complicates this learning process.

To address memory requirements, our proposed 1.5 mm model consists of two models with 28 classes each. We also trained a single model with all 56 classes, which performed slightly worse, indicating that a lower number of classes can facilitate learning. The complete results of the ablation study are presented in Table 3.

	Nr of classes	Dice	NSD
MR test set			
trained on MR + CT	56	0.827 [CI: 0.803, 0.847]	0.894 [CI: 0.870, 0.913]
trained on MR	56	0.808 [CI: 0.781, 0.833]	0.874 [CI: 0.847, 0.896]
trained on CT	56	0.000 [CI: 0.000, 0.000]	0.000 [CI: 0.000, 0.002]
trained on MR + CT; single model	56	0.821 [CI: 0.794, 0.842]	0.885 [CI: 0.860, 0.905]
CT test set			
trained on MR + CT	56	0.960 [CI: 0.959, 0.962]	0.994 [CI: 0.993, 0.994]
trained on MR	56	0.648 [CI: 0.634, 0.662]	0.648 [CI: 0.636, 0.661]
trained on CT	56	0.967 [CI: 0.966, 0.969]	0.995 [CI: 0.995, 0.996]
trained on MR + CT; single model	56	0.955 [CI: 0.953, 0.956]	0.992 [CI: 0.991, 0.993]

Table 3: Overview of ablation study results. (NSD: Normalised Surface Distance; CI: 95% Confidence Interval).

3.4. Failure cases

In the MRI test set, we observed clearly lower Dice scores compared to the CT test set. This discrepancy is primarily due to the inferior image quality of MR images. Many MR images exhibit high anisotropy, with slice thicknesses exceeding 6 mm, making it challenging to detect small structures such as the iliac arteries and veins, even for the human eye. Additionally, other MR images display low contrast outside the area of interest, further complicating the identification of structures in these regions. Figure 5 shows some examples.

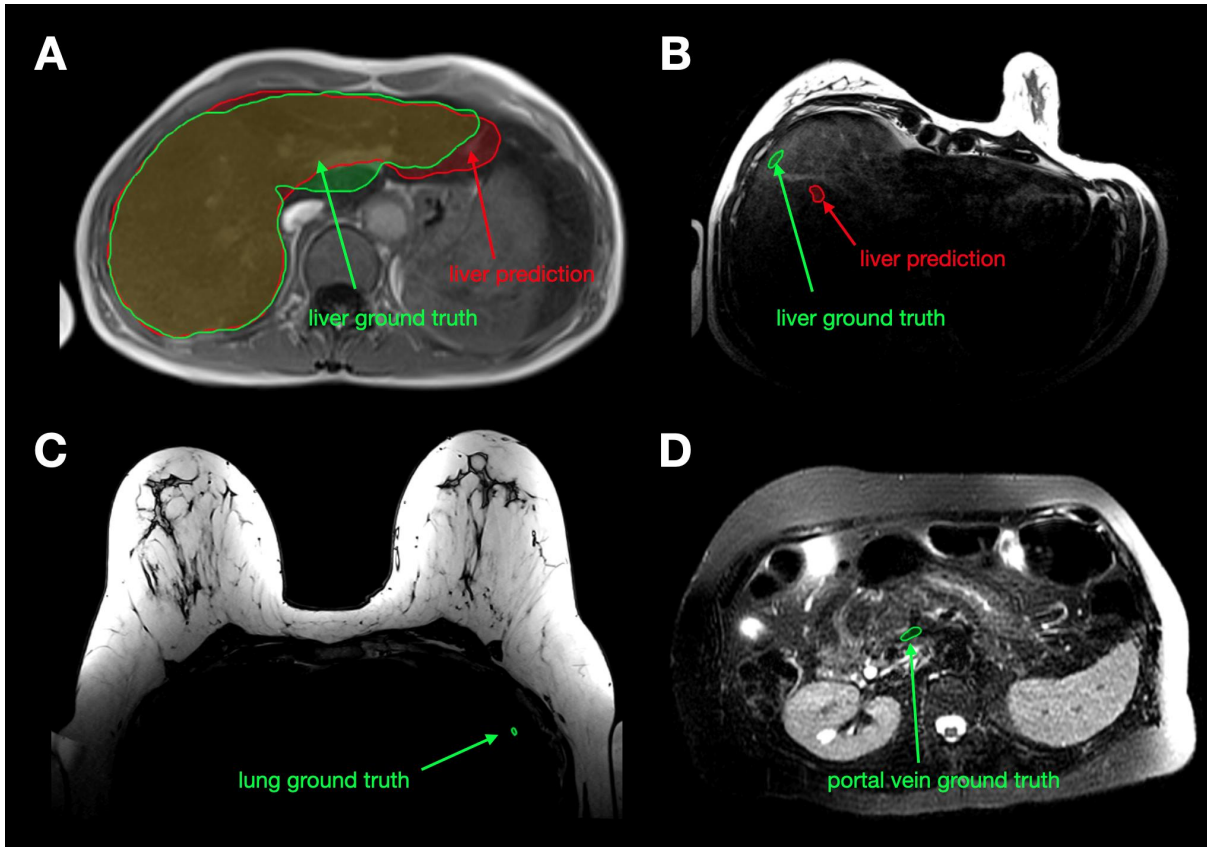


Figure 5: Examples of failure cases from the MR test set. A: The exact border of the liver is hard to see. Both the ground truth and the prediction could be correct. B: The abdomen contains little contrast since this examination focused on the breasts. Therefore, both the ground truth and the prediction could not find any proper liver. For the ground truth it would have been better to segment nothing instead of only a small random patch. This is an example of errors in the ground truth. C: As in case B this examination has little contrast in the thorax and therefore errors in the lung segmentation. D: The portal vein is difficult to see in this image. Therefore, the ground truth segmentation was incomplete, and the prediction was completely empty.

3.5. Runtime

Since our model uses the same nnU-Net architecture and the same baseline resolution of 1.5 mm and 3 mm as TotalSegmentator for CT, for runtime and memory requirements, we refer to the original TotalSegmentator paper (3).

4. Discussion

In this study, we trained a robust model, TotalSegmentator MRI, on a diverse dataset containing different MR sequences and anatomical regions, and that is able to automatically segment 59 anatomical structures with high accuracy. Our proposed model is clinically representative, easy to use, fast to run, and achieved good performance across most classes. It significantly outperformed two other publicly available models. We have shared our model, the training dataset and also the annotations.

Since the introduction of TotalSegmentator CT (3), the demand for a robust model capable of automatically segmenting multiple structures in MR images has increased (4). Following the similar

iterative workflow that we had previously introduced with the TotalSegmentator CT, we developed the TotalSegmentator MRI.

Recently, several new studies on automatic MRI segmentation have been published, but most have not shared their model and data (8,12-14). Among these, only one study has made their model, MRSegmentator, available, but the authors did not share their training data or annotations (8). Our TotalSegmentator MRI model offers clear advantages over this new model as it can segment more structures and was trained on a more diverse clinical dataset. Although the segmentation performance of MRSegmentator was 2 Dice points higher for abdominal organs, TotalSegmentator MRI outperformed MRSegmentator on the other anatomical structures. In addition, we have made both our dataset and annotations publicly available, unlike previous state-of-the-art models.

Our study has several limitations. First, the current proposed model did not achieve a Dice score over 0.9, primarily due to the lower resolution and quality of most MR images. But also, errors in the ground truth annotations reduced the accuracy. While TotalSegmentator CT can automatically segment more structures, our current model features the highest number of structures among those specifically designed for MR segmentation. Despite this, we plan to enhance TotalSegmentator MRI by adding more structures, improving the quality of the ground truth annotations and expanding our training dataset.

In conclusion, we have developed an open-source, easy-to-use model that can robustly and rapidly segment MR images and could be employed both in clinical and in research projects. The code (<https://github.com/wasserth/TotalSegmentator>) and data (<https://zenodo.org/doi/10.5281/zenodo.11367004>) are publicly available.

5. References

1. Isensee F, Jaeger PF, Kohl SAA, Petersen J, Maier-Hein KH. nnU-Net: a self-configuring method for deep learning-based biomedical image segmentation. *Nat Methods*. 2021 Feb;18(2):203–11.
2. Isensee F, Petersen J, Klein A, Zimmerer D, Jaeger PF, Kohl S, et al. nnU-Net: Self-adapting Framework for U-Net-Based Medical Image Segmentation. *arXiv*. 2018;
3. Wasserthal J, Breit H-C, Meyer MT, Pradella M, Hinck D, Sauter AW, et al. Totalsegmentator: robust segmentation of 104 anatomic structures in CT images. *Radiol Artif Intell*. 2023 Sep;5(5):e230024.
4. Pickhardt PJ, Summers RM, Garrett JW, Krishnaraj A, Agarwal S, Dreyer KJ, et al. Opportunistic screening: radiology scientific expert panel. *Radiology*. 2023 Jun;307(5):e222044.
5. Fischl B, Salat DH, van der Kouwe AJW, Makris N, Ségonne F, Quinn BT, et al. Sequence-independent segmentation of magnetic resonance images. *Neuroimage*. 2004;23 Suppl 1:S69-84.
6. Fedorov A, Longabaugh WJR, Pot D, Clunie DA, Pieper SD, Gibbs DL, et al. National cancer institute imaging data commons: toward transparency, reproducibility, and scalability in imaging artificial intelligence. *Radiographics*. 2023 Dec;43(12):e230180.
7. Hoopes A, Mora JS, Dalca AV, Fischl B, Hoffmann M. SynthStrip: skull-stripping for any brain image. *Neuroimage*. 2022 Oct 15;260:119474.
8. Häntze H, Xu L, Dorfner FJ, Donle L, Truhn D, Aerts H, et al. MRSegmentator: Robust Multi-

- Modality Segmentation of 40 Classes in MRI and CT Sequences. arXiv. 2024;
9. Reinke A, Tizabi MD, Baumgartner M, Eisenmann M, Heckmann-Nötzel D, Kavur AE, et al. Understanding metric-related pitfalls in image analysis validation. *Nat Methods*. 2024 Feb 12;21(2):182–94.
 10. Maier-Hein L, Reinke A, Godau P, Tizabi MD, Buettner F, Christodoulou E, et al. Metrics reloaded: recommendations for image analysis validation. *Nat Methods*. 2024 Feb 12;21(2):195–212.
 11. Ji Y, Bai H, Yang J, Ge C, Zhu Y, Zhang R, et al. AMOS: A Large-Scale Abdominal Multi-Organ Benchmark for Versatile Medical Image Segmentation. arXiv. 2022;
 12. Zhou A, Liu Z, Tieu A, Patel N, Sun S, Yang A, et al. MRAnnotator: A Multi-Anatomy Deep Learning Model for MRI Segmentation. arXiv. 2024;
 13. Ciausiu C, Krishnaswamy D, Billot B, Pieper S, Kikinis R, Fedorov A. Towards Automatic Abdominal MRI Organ Segmentation: Leveraging Synthesized Data Generated From CT Labels. arXiv. 2024;
 14. Zhuang Y, Mathai TS, Mukherjee P, Khoury B, Kim B, Hou B, et al. MRISegmentator-Abdomen: A Fully Automated Multi-Organ and Structure Segmentation Tool for T1-weighted Abdominal MRI. arXiv. 2024;
 15. Erickson BJ, Kirk S, Lee Y, Bathe O, Kearns M, Gerdes C, et al. Radiology Data from The Cancer Genome Atlas Liver Hepatocellular Carcinoma [TCGA-LIHC] collection. The Cancer Imaging Archive. 2016;
 16. Vallières M, Freeman CR, Skamene SR, El Naqa I. A radiomics model from joint FDG-PET and MRI texture features for the prediction of lung metastases in soft-tissue sarcomas of the extremities. *Phys Med Biol*. 2015 Jul 21;60(14):5471–96.
 17. National Cancer Institute Clinical Proteomic Tumor Analysis Consortium (CPTAC). Radiology Data from the Clinical Proteomic Tumor Analysis Consortium Clear Cell Renal Cell Carcinoma [CPTAC-CCRCC] collection. The Cancer Imaging Archive. 2018;
 18. Kirk S, Lee Y, Lucchesi FR, Aredes ND, Grusauskas N, Catto J, et al. Radiology Data from The Cancer Genome Atlas Urothelial Bladder Carcinoma [TCGA-BLCA] collection. The Cancer Imaging Archive. 2016;
 19. Linehan M, Gautam R, Kirk S, Lee Y, Roche C, Bonaccio E, et al. Radiology Data from The Cancer Genome Atlas Cervical Kidney renal papillary cell carcinoma [KIRP] collection. The Cancer Imaging Archive. 2016;
 20. Akin O, Elnajjar P, Heller M, Jarosz R, Erickson BJ, Kirk S, et al. Radiology Data from The Cancer Genome Atlas Kidney Renal Clear Cell Carcinoma [TCGA-KIRC] collection. The Cancer Imaging Archive. 2016;
 21. Kinahan P, Muzi M, Bialecki B, Herman B, Coombs L. Data from the ACRIN 6668 Trial NSCLC-FDG-PET. The Cancer Imaging Archive. 2019;
 22. National Cancer Institute Clinical Proteomic Tumor Analysis Consortium (CPTAC). The Clinical Proteomic Tumor Analysis Consortium Sarcomas Collection (CPTAC-SAR). The Cancer Imaging Archive. 2019;
 23. Rozenfeld M, Jordan P. Annotations for The Clinical Proteomic Tumor Analysis Consortium Clear Cell Renal Cell Carcinoma Collection (CPTAC-CCRCC-Tumor-Annotations). The

- Cancer Imaging Archive. 2023;
24. National Cancer Institute Clinical Proteomic Tumor Analysis Consortium (CPTAC). Radiology Data from the Clinical Proteomic Tumor Analysis Consortium Pancreatic Ductal Adenocarcinoma [CPTAC-PDA] Collection. The Cancer Imaging Archive. 2018;
 25. Rozenfeld M, Jordan P. Annotations for The Clinical Proteomic Tumor Analysis Consortium Pancreatic Ductal Adenocarcinoma Collection (CPTAC-PDA-Tumor-Annotations). The Cancer Imaging Archive. 2023;
 26. Linehan MW, Gautam R, Sadow CA, Levine S. Radiology Data from The Cancer Genome Atlas Kidney Chromophobe [TCGA-KICH] collection. The Cancer Imaging Archive. 2016;
 27. Roche C, Bonaccio E, Filippini J. Radiology Data from The Cancer Genome Atlas Sarcoma [TCGA-SARC] collection. The Cancer Imaging Archive. 2016;
 28. National Cancer Institute Clinical Proteomic Tumor Analysis Consortium (CPTAC). Radiology Data from the Clinical Proteomic Tumor Analysis Consortium Lung Adenocarcinoma [CPTAC-LUAD] collection. The Cancer Imaging Archive. 2018;
 29. National Cancer Institute Clinical Proteomic Tumor Analysis Consortium (CPTAC). Radiology Data from the Clinical Proteomic Tumor Analysis Consortium Cutaneous Melanoma [CPTAC-CM] collection. The Cancer Imaging Archive. 2018;
 30. Saltz J, Saltz M, Prasanna P, Moffitt R, Hajagos J, Bremer E, et al. Stony Brook University COVID-19 Positive Cases. The Cancer Imaging Archive. 2021;
 31. Biobank CM. Cancer Moonshot Biobank - Lung Cancer Collection (CMB-LCA). The Cancer Imaging Archive. 2022;
 32. Biobank CM. Cancer Moonshot Biobank - Multiple Myeloma Collection (CMB-MML). The Cancer Imaging Archive. 2022;
 33. Biobank CM. Cancer Moonshot Biobank - Colorectal Cancer Collection (CMB-CRC). The Cancer Imaging Archive. 2022;
 34. Rutherford M, Mun SK, Levine B, Bennett W, Smith K, Farmer P, et al. A DICOM dataset for evaluation of medical image de-identification. *Sci Data*. 2021 Jul 16;8(1):183.
 35. Van Oss J, Murugesan GK, McCrumb D, Soni R. Image segmentations produced by BAMF under the AIMI Annotations initiative. Zenodo. 2023;

6. Supplemental Materials

S1: List of all segmented structures

spleen, kidney right, kidney left, gallbladder, liver, stomach, pancreas, adrenal gland right, adrenal gland left, lung left, lung right, esophagus, small bowel, duodenum, colon, urinary bladder, prostate, sacrum, vertebrae, intervertebral discs, spinal cord, heart, aorta, inferior vena cava, portal vein and splenic vein, iliac artery left, iliac artery right, iliac vena left, iliac vena right, humerus left, humerus right, fibula, tibia, femur left, femur right, hip left, hip right, gluteus maximus left, gluteus maximus right, gluteus medius left, gluteus medius right, gluteus minimus left, gluteus minimus right, autochthon left, autochthon right, iliopsoas left, iliopsoas right, quadriceps femoris left, quadriceps femoris right, thigh medial compartment left, thigh medial compartment right, thigh posterior compartment left, thigh posterior compartment right, sartorius left, sartorius right, brain, subcutaneous fat, skeletal muscle, torso fat.

S2: List of all pretrained models which were used during the data annotation

Name: synthstrip (<https://surfer.nmr.mgh.harvard.edu/docs/synthstrip/>)

Classes: brain

Name: <https://doi.org/10.1186/s12880-023-01056-9>

Classes: gluteus left, gluteus right, quadriceps femoris left, quadriceps femoris right

Name: MRSegmentator (<https://github.com/hhaentze/MRSegmentator>)

Classes: gallbladder, stomach, adrenal gland right, adrenal gland left, small bowel, duodenum, colon, portal vein and splenic vein, iliac artery left, iliac artery right, iliac vena left, iliac vena right

S3: List of segmented structures for comparison to MRSegmentator and AMOS model

MRSegmentator (40 structures): spleen, kidney right, kidney left, gallbladder, liver, stomach, pancreas, adrenal gland right, adrenal gland left, lung left, lung right, heart, aorta, inferior vena cava, portal vein and splenic vein, iliac artery left, iliac artery right, iliac vena left, iliac vena right, esophagus, small bowel, duodenum, colon, urinary bladder, vertebrae, sacrum, hip left, hip right, femur left, femur right, autochthon left, autochthon right, iliopsoas left, iliopsoas right, gluteus maximus left, gluteus maximus right, gluteus medius left, gluteus medius right, gluteus minimus left, gluteus minimus right

AMOS (13 structures): spleen, kidney right, kidney left, gallbladder, liver, stomach, pancreas, adrenal gland right, adrenal gland left, esophagus, duodenum, aorta, inferior vena cava

S4: List of sources of external IDC datasets

1. Radiology Data from The Cancer Genome Atlas Liver Hepatocellular Carcinoma [TCGA-LIHC] collection (15)
2. A radiomics model from joint FDG-PET and MRI texture features for the prediction of lung metastases in soft-tissue sarcomas of the extremities (16)
3. Radiology Data from the Clinical Proteomic Tumor Analysis Consortium Clear Cell Renal Cell Carcinoma [CPTAC-CCRCC] collection (17)
4. Radiology Data from The Cancer Genome Atlas Urothelial Bladder Carcinoma [TCGA-BLCA] collection (18)
5. Radiology Data from The Cancer Genome Atlas Cervical Kidney renal papillary cell carcinoma [KIRP] collection (19)
6. Radiology Data from The Cancer Genome Atlas Kidney Renal Clear Cell Carcinoma [TCGA-KIRC] collection (20)
7. Data from the ACRIN 6668 Trial NSCLC-FDG-PET (21)
8. The Clinical Proteomic Tumor Analysis Consortium Sarcomas Collection (CPTAC-SAR) (22)
9. Annotations for The Clinical Proteomic Tumor Analysis Consortium Clear Cell Renal Cell Carcinoma Collection (CPTAC-CCRCC-Tumor-Annotations) (23)
10. Radiology Data from the Clinical Proteomic Tumor Analysis Consortium Pancreatic Ductal Adenocarcinoma [CPTAC-PDA] Collection (24)
11. Annotations for The Clinical Proteomic Tumor Analysis Consortium Pancreatic Ductal Adenocarcinoma Collection (CPTAC-PDA-Tumor-Annotations) (25)
12. Radiology Data from The Cancer Genome Atlas Kidney Chromophobe [TCGA-KICH] collection (26)
13. Radiology Data from The Cancer Genome Atlas Sarcoma [TCGA-SARC] collection (27)
14. Radiology Data from the Clinical Proteomic Tumor Analysis Consortium Lung Adenocarcinoma [CPTAC-LUAD] collection (28)
15. Radiology Data from the Clinical Proteomic Tumor Analysis Consortium Cutaneous Melanoma [CPTAC-CM] collection (29)
16. Stony Brook University COVID-19 Positive Cases (30)
17. Cancer Moonshot Biobank - Lung Cancer Collection (CMB-LCA) (31)
18. Cancer Moonshot Biobank - Multiple Myeloma Collection (CMB-MML) (32)
19. Cancer Moonshot Biobank - Colorectal Cancer Collection (CMB-CRC) (33)
20. A DICOM dataset for evaluation of medical image de-identification (Pseudo-PHI-DICOM-Data) (34)
21. Image segmentations produced by BAMF under the AIMI Annotations initiative (35)
22. National cancer institute imaging data commons: toward transparency, reproducibility, and scalability in imaging artificial intelligence. (6)

S5: Training details

The following adaptations to the default nnU-Net settings were applied: First, mirroring was removed from the data augmentation pipeline because otherwise, the model was not able to properly distinguish between left and right anatomical structures. Second, the resampling interpolation for the segmentation masks was set to order 0 for faster training. Normalization was set to “MR” for all our experiments even when only training on CT images.

Training one nnU-Net model for all 56 classes at the same time results in very high memory consumption. Thus, we split the 56 classes into two parts each with 28 classes. For each part, one smaller nnU-Net was trained.

For the 3 mm model it was possible to combine all 56 classes into one model without unreasonable memory requirements.

S6. Supplemental Figures



Figure S1: Overview of results of our model for each anatomical structure, sorted by Dice score. The coloured dots show the median, the grey dots show the results for each subject.